XIV. PLASMA ELECTRONICS[*]

Prof. L. D. Smullin
Prof. H. A. Haus
Prof. A. Bers
Prof. W. D. Getty
Prof. D. J. Rose
Prof. T. H. Dupree
Prof. L. M. Lidsky
Prof. E. P. Gyftopoulos
Dr. G. Fiocco
F. Alvarez de Toledo
W. L. Brassert
R. J. Briggs

J. R. Cogdell
L. J. Donadieu
S. A. Evans
B. A. Hartenbaum
W. G. Homeyer
H. Y. Hsieh
A. J. Impink, Jr.
P. K. Karvellas
J. D. Levine
L. N. Lontai
D. L. Morse
R. T. Nowak

L. M. Petrie, Jr.
W. D. Rummler
A. J. Schneider
P. E. Serafim
P. S. Spangler
G. Theodoridis
E. Thompson
J. S. Tulenko
C. E. Wagner
S. Wilensky
H. L. Witting
J. C. Woo

RESEARCH OBJECTIVES

1. Plasmas for Electrical Energy Conversion

The group working in plasma electronics is concerned with the synthesizing or design of particular plasma systems to perform specified functions. The research program described below is primarily concerned with the plasma as a component of a power generator: either controlled thermonuclear fusion or magnetohydrodynamic. To this end, we are studying several methods of producing and containing dense, hot plasmas. We are also concerned with the collective behavior of plasmas of finite dimensions, and are studying possible means of energy extraction. Thus we are led to the investigation of MHD waves on moving plasma streams, and of waves in plasma waveguides and their stability.

Beam-Plasma Discharge. During the past year we have shown that a relatively dense plasma can be produced by an electron beam injected into a low-pressure drift region. This phenomenon is basically a microwave discharge, in which the strong microwave fields are produced by the interaction between the beam and the plasma already present. With a 10-kv, 1-amp, 100-μsec pulsed beam, plasmas of $5 \times 10^{12}/cm^3$ density and very high electron temperatures have been produced.

During the coming year we shall extend this work, using more powerful beams (10-kv, 10-amps from a magnetron injection gun), and injected molecular beams. These techniques should allow us to approach 100 per cent ionization, and we should begin to see relatively high-temperature ions as a result of ohmic heating. We shall have four experiments running, devoted to the detailed study of various aspects of the beam-plasma discharge.

L. D. Smullin, W. D. Getty

Electron Cyclotron Resonant Discharge. Our preliminary experiments, using ~ 0.5 Mw of 10-cm power, have resulted in producing an intense discharge from which 2-Mev x-rays emanate. Because of lack of room for suitable shielding, the experiments were temporarily abandoned. We are now rebuilding our high-power experiment in another wing of the Research Laboratory of Electronics, where suitable shielding can

be installed; and, a low-power (~ 100 kw) system is also being assembled. An analog computer program is being developed for studying electron trajectories under the influence of an rf field and a mirror (nonuniform) magnetostatic field.

D. J. Rose, L. D. Smullin, G. Fiocco

Thomson Scattering of Light from Electrons. The first laboratory observation of light scattering by electrons was made in the Research Laboratory of Electronics in November 1962, by using a laser beam. During the coming year, we plan to develop this technique into a useful tool for plasma diagnostics.

G. Fiocco, E. Thompson

Theory of Active and Passive Anisotropic Waveguides. The work on this topic will proceed along two lines:

(i) Development of small-signal energy and momentum-conservation principles that are applicable to the linearized equations of anisotropic waveguides in the absence of loss. These are used to obtain criteria for the stability or amplifying nature of the waves in these systems.

(ii) Analysis of specific waveguides of current interest, and determination of their dispersion characteristics.

The dispersion characteristics may be also used to test the general criteria obtained from the conservation principles.

A. Bers, H. A. Haus

Magnetohydrodynamics Power Generation. We are studying the possibilities of energy extraction from moving fluids through coupling of circuit fields to the waves in the fluid. Both the linearized problem in two or three dimensions, and the nonlinear equations in a one-dimensional geometry are being studied; effects attributable to variation of geometric parameters are sought from the former, saturation effects and efficiences are studied through the latter.

H. A. Haus

2. Highly Ionized Plasma and Fusion Research

Plasma Kinetic Theory. Methods of solving the plasma kinetic equations, including the presence of self-generated and externally applied electromagnetic fields, are being successfully developed. This work, which leads to rigorous predictions of plasma properties, will be continued and extended.

T. H. Dupree

Charged-Particle Confinement by Nonadiabatic Motion. Injection of ions or electrons into a magnetic mirror or other confining structure by spatially resonant field perturbations is a continuing project. A 3-meter long experiment for trapping electrons in a mirror field (200 gauss central section) is being constructed, and the theories of initial trapping and eventual confinement time are being refined.

L. M. Lidsky, D. J. Rose

Superconducting Magnets. A large superconducting magnet (room-temperature working space, 0.05 m^3) will be completed early this year; engineering design principles that have been worked out for such systems have been reported, and the magnet itself is expected to be used for plasma-confinement experiments. Studies of field quenching, parasitic diamagnetic current generation, and general operating behavior of the magnet

in various field configurations will be carried out.

D. J. Rose

Thermonuclear-Blanket Studies. Calculations carried out over the past year on neutron slowing down, neutron multiplication, tritium regeneration, heat transfer, and energy recovery are being extended to include other important effects. Principal effects are: addition of fissionable materials, gamma transport, and coil shielding. Experiments with 14 Mev neutrons from Van de Graaf D-T reactions on fusion blanket mock-up assemblies continue.

D. J. Rose, I. Kaplan

Cesium Plasmas. With a view to eventual electrical energy conversion from nuclear heat and other prime sources, the physical properties of the cesium plasma itself and a number of experimental devices are being studied.

E. P. Gyftopoulos

Arc-Plasma Studies. The hollow-cathode source previously developed and reported on will be used to generate plasmas in the density range $10^{15}/cm^3$, 90-95 per cent ionized by pulse techniques, to study plasma stability in long plasma columns, and to obtain a "standard" for comparison of diagnostic methods.

L. M. Lidsky

A. NONLINEAR ONE-DIMENSIONAL MAGNETOHYDRODYNAMIC MONOTRON

A linearized analysis of the one-dimensional magnetohydrodynamic (MHD) monotron has previously been carried out by Haus.[1] The present work involves a nonlinear analysis of the same device. The amplitude of the oscillations as limited by the nonlinearities can be determined, and, in particular, the efficiency of the device as an energy converter can be obtained. We have been able to solve the problem of the nonlinear one-dimensional MHD monotron of the same geometry as that of Haus[1] when the coil is terminated by a parallel combination of a load conductance and a sinusoidal current source (exciter), under the following assumed conditions: (a) the ratio of the specific heats of
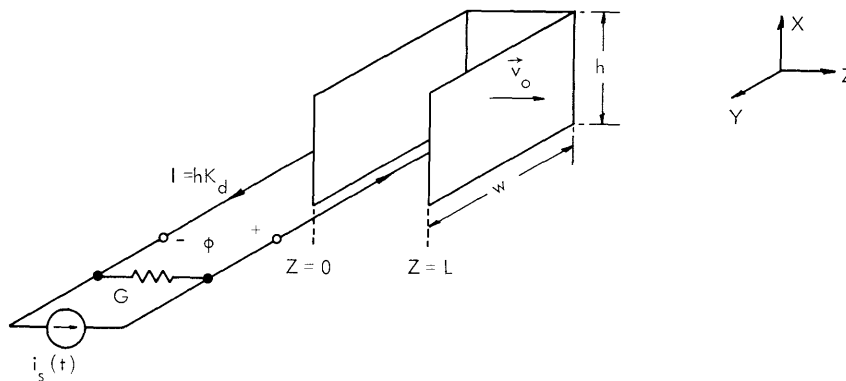

Fig. XIV-1. Monotron connected to external circuit.

the fluid is 2; (b) the flow remains supercritical throughout the entire flow field; and (c) the fluid is unperturbed at t = 0.

The monotron connected to the external circuit is shown in Fig. XIV-1. The sheets coupling to the fluid carry current of density K_d and the terminal current is thus $I = hK_d$.

For $\gamma = 2$, the normalized equations of motion for the fluid are

$$\frac{\partial V}{\partial T} + V\frac{\partial V}{\partial Z} + \bar{c}^2\frac{\partial R}{\partial Z} = J \tag{1}$$

$$\frac{\partial R}{\partial T} + \frac{\partial(VR)}{\partial Z} = 0, \tag{2}$$

in which the normalized variables are $Z = \frac{\omega}{v_o} z$, $T = \omega t$, $V(Z,T) = \frac{v}{v_o}$, $R(Z,T) = \frac{\rho}{\rho_o}$, $\bar{c} = \frac{c}{v_o}$, and $J = \frac{B_o}{\omega\rho_o v_o} J_d$ is the normalized driving current density. Here, v_o and ρ_o are the entry velocity and the entry density, respectively, c is the small-signal magnetoacoustic speed, and ω is the frequency of the source. Equations 1 and 2 can be obtained, for example, by combining Eqs. 1-6 of Haus and Schneider.[2]

A completely equivalent description of the fluid is provided by the so-called characteristic equations,[3] which are essentially linear combinations of Eqs. 1 and 2 arranged to place in evidence the fast- and slow-wave nature of the solution.

$$\frac{\partial}{\partial T}(V+2C) + (V+C)\frac{\partial}{\partial Z}(V+2C) = J \tag{3}$$

$$\frac{\partial}{\partial T}(V-2C) + (V-C)\frac{\partial}{\partial Z}(V-2C) = J \tag{4}$$

Here, $C = \bar{c}\sqrt{R}$ is the local magnetoacoustic speed. Except for the current terms on the right-hand side, these equations are identical with those describing the propagation of water (gravity) waves in shallow water. Indeed, our study of the special case $\gamma = 2$ was prompted in part by noting this similarity.

To obtain boundary conditions, we study the effect wrought on the fluid by the current sheets. When Eqs. 1 and 2 are integrated across each of the current sheets, we obtain

$$\left(\frac{V_2^2}{2} + \bar{c}^2 R_2\right) - \left(\frac{V_1^2}{2} + \bar{c}^2 R_1\right) = K \tag{5}$$

$$V_2 R_2 - V_1 R_1 = 0 \tag{6}$$

$$\left(\frac{V_4^2}{2} + \bar{c}^2 R_4\right) - \left(\frac{V_3^2}{2} + \bar{c}^2 R_3\right) = -K \tag{7}$$

$$V_4 R_4 - V_3 R_3 = 0. \tag{8}$$

The subscripts 1, 2, 3, and 4 indicate that the quantities are evaluated at $Z = 0-$, $Z = 0+$, $Z = L-$, and $Z = L+$, respectively. The normalized sheet current density is given by

$$K = \frac{B_o}{\rho_o v_o^2} K_d.$$

Provided that both the fast and slow waves at $Z = 0+$ are forward waves, the fluid upstream from the current sheet is unaffected, and thus $V_1 = 1$ and $R_1 = 1$. The normalized terminal voltage $\Phi = \frac{\phi}{B_o v_o w}$ is given by

$$\Phi = 1 - V_3 R_3. \tag{9}$$

The circuit, a conductance G in parallel with an exciting current source $i_s(T) = I \sin T$, has the volt-ampere relation

$$I \sin T = hK_d + wv_o B_o G\Phi. \tag{10}$$

The combination of Eqs. 5, 6, 9, and 10 furnishes the relation that expresses the effect of the circuit upon the fluid:

$$V_2^2 + \{2P(1-V_3R_3)-(1+2\bar{c}^2)-2S \sin T\} V_2 + 2\bar{c}^2 = 0. \tag{11}$$

The fact that the fluid velocity at $Z = 0$ must be continuous in the limit of zero sheet current requires that the largest positive real root of the cubic equation for V_2 be chosen. The parameter $S = \frac{B_o}{\rho_o v^2 h} I$ expresses the strength of the source; $P = \left(\frac{w}{h}\right)\frac{B_o^2 G}{\rho_o v_o}$ expresses the magnitude of the load.

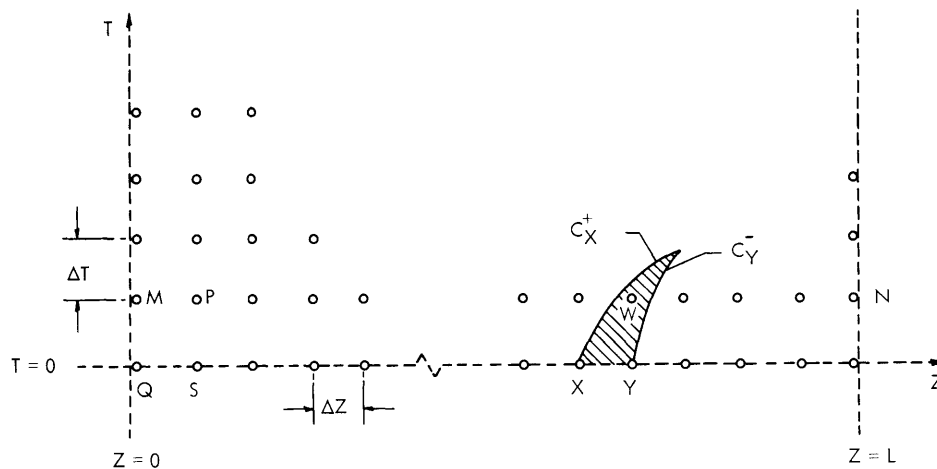The behavior of the monotron is determined by either Eqs. 1 and 2, or Eqs. 3 and 4,

Fig. XIV-2. Lattice points that are pertinent to a numerical
solution by finite differences of Eqs. 3 and 4.

with J set equal to zero, by Eq. 11, and by the initial conditions V(Z, 0) = R(Z, 0) = 1. The regime of operation is determined by the requirement that the flow be supercritical everywhere or, in other words, that the slow wave be a forward wave. The wave equation (4) indicates that the velocity of the slow wave is $V - \bar{c}\sqrt{R}$; we thus require that $(V-\bar{c}\sqrt{R})$ be greater than zero everywhere.

To obtain numerical solutions, we have replaced the partial derivatives in Eqs. 3 and 4 by difference quotients appropriate to a rectangular net of points spanning the region of interest $(0<Z<L, 0 \leqslant T<\infty)$ in the Z-T plane (Fig. XIV-2). The resulting difference equations and Eq. 11 allow the computations to begin at T = 0 with the given initial conditions and progress into the region in the direction of increasing T.

With reference to Fig. XIV-2, the difference equations relate the values of V and R at point P, for example, to the values of V and R at points Q and S. Since V and R are each equal to unity along the entire bottom row (T=0), the difference equations allow the values of V and R to be obtained for every lattice point of the second row, with the exception of the leftmost point, point M. The value at this point can be obtained, however, from the values at point N by means of the boundary condition, Eq. 11. With the second row completely determined, the values for the third row can be found, and so forth.

The lattice spacing in the Z-direction is fixed; the lattice spacing in the T-direction is adjusted at each stage as the computations proceed in order to ensure that the lattice point at which the values of V and R are to be found lies within the region of determinacy of the lattice points used in the calculation. Again, with reference to Fig. XIV-2, ΔT must be chosen small enough so that the lattice point W, for example, whose values of V and R are to be found from those at lattice points X and Y, lies in the shaded region defined by the fast-wave characteristic C_X^+ emanating from point X and the slow-wave characteristic C_Y^- emanating from point Y. This has been shown to be the condition
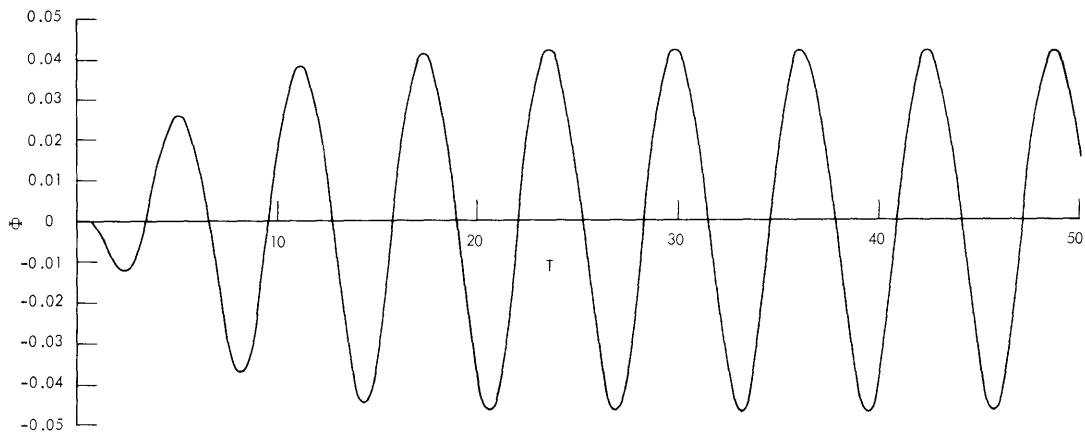

Fig. XIV-3. Typical terminal voltage waveform.

for which the solution of the difference equations converges to the solution of the differential equations in the limit of zero mesh spacing.[4,5] It is apparent that for this scheme to work, the flow must be supercritical so that the slope of the $C_{\bar{Y}}$ characteristic is positive.

In order to provide the most favorable conditions for energy conversion, the coil span L was chosen so that the terminal impedance of the monotron, as determined by small-signal analysis,[1] was negative real.

A typical terminal voltage waveform is shown in Fig. XIV-3. For this case the entry velocity was taken to be twice the magnetoacoustic speed (c=0.5), S = 0.01, P = 0.5 and $\omega L/v_o$ = $3\pi/8$. If an efficiency of energy conversion is defined as the ratio of the average electric power extracted from the fluid to the mechanical power incident on the monotron at Z = 0, the efficiency for the case illustrated is found to be 0.1 per cent, a very low value indeed. Note, too, the almost sinusoidal shape of the steady-state waveform. Indeed, for all allowed values of S and P, that is, all values that lead to solutions satisfying assumption (b), the steady-state output waveforms are sinusoidal in appearance and yield very low values of efficiency. We conclude that the regime studied is still essentially a linear one. In further work we shall attempt to remove the restriction that the flow be supercritical everywhere. This will undoubtedly lead to more distorted waveforms accompanied, we trust, by higher efficiencies.

The numerical calculations for the work described here were performed on the IBM 7090 computer of the Computation Center, M.I.T.

A. J. Schneider

References

1. H. A. Haus, Magnetohydrodynamic Monotrons, Internal Memorandum, Research Laboratory of Electronics, M.I.T., April 1961.

2. H. A. Haus and A. J. Schneider, A large-signal, steady-state solution for a one-dimensional plasma coupled to a traveling-wave circuit, Quarterly Progress Report No. 64, Research Laboratory of Electronics, M.I.T., January 15, 1962, pp. 90-92.

3. J. J. Stoker, Water Waves (Interscience Publishers, New York, 1957), p. 469 ff.

4. Ibid., p. 474 ff.

5. R. Courant, E. Isaacson, and M. Rees, On the solution of nonlinear hyperbolic differential equations by finite differences, Communs. Pure and Appl. Math. 5, 243 (1952).

B. AN ALTERNATIVE PROOF OF STABILITY FOR THE MAGNETOHYDRODYNAMIC WAVEGUIDE

It was shown in an earlier report[1] that the magnetohydrodynamic (MHD) waveguide is stable for all geometric configurations and for all values of the parameters describing the MHD beam. The proof given there involved an investigation of the two types of modes

that can exist in such a waveguide. It was shown that the dispersion relation for one set of modes and the boundary conditions for the other set admit of only stable solutions. It can be shown that these results follow more simply from an investigation of the form of the power theorem that all solutions must satisfy. In this report we present the simpler stability proof to confirm the earlier one and to show again the importance of small-signal power theorems.

In the equations and boundary conditions relevant to the MHD waveguide, the frequency ω and the dc beam velocity v_o appear only in the combination $\omega_r = \omega - \beta v_o$, which is the frequency in a coordinate system moving with beam velocity. We can, therefore, always transform the equations into a coordinate system in which the beam is stationary without changing their form. A system is stable if the energy term in its small-signal power theorem (provided that it satisfies a power theorem) is positive definite[2] since, in that case, all real values of β require real values of ω_r. The energy term in the MHD power theorem[3] is

$$w = w_m + w_k = \frac{1}{2\mu_o} \overline{B} \cdot \overline{B} + \frac{1}{2} \rho_o \overline{v} \cdot \overline{v} + (\overline{v}_o \cdot \overline{v})\rho + \frac{\rho\rho}{2\rho_o} + \frac{\rho_o v_o}{B_o} \overline{B} \cdot \overline{v},$$

which is positive definite when v_o is set equal to zero. (Note that in Quarterly Progress Report No. 66 (page 125), Eq. 9 and the equations for S_K and w_k are in error. The term $(v_o/B_o)\overline{B} \cdot \overline{v}$ should be $\rho_o(v_o/B_o)\overline{B} \cdot \overline{v}$.) Thus, ω_r (and, therefore, ω) is real for all real β, and according to Sturrock[4] this is a sufficient condition for stability.

J. R. Cogdell

References

1. J. R. Cogdell, A stability proof for magnetohydrodynamic waveguides, Quarterly Progress Report No. 67, Research Laboratory of Electronics, M.I.T., October 15, 1962, pp. 76-79.

2. For a discussion of this application of the small-signal power theorem, see H. A. Haus, Small Signal Conservation Theorems, a paper presented at the Symposium on Plasma Physics, Faculté des Sciences, Orsay, France, September 10-21, 1962.

3. J. R. Cogdell, A magnetohydrodynamic small-signal power theorem, Quarterly Progress Report No. 66, Research Laboratory of Electronics, M.I.T., July 15, 1962, pp. 123-129.

4. P. A. Sturrock, Kinematics of growing waves, Phys. Rev. 112, 1488-1503 (1958).

C. SCATTERING OF LIGHT FROM ELECTRONS II

Using the apparatus indicated in Fig. XIV-4, we have observed scattering of optical radiation from an electron beam. Light from a ruby laser was focused to intersect an electron beam at right angles and the scattered radiation was observed at an angle $\theta = 65°$
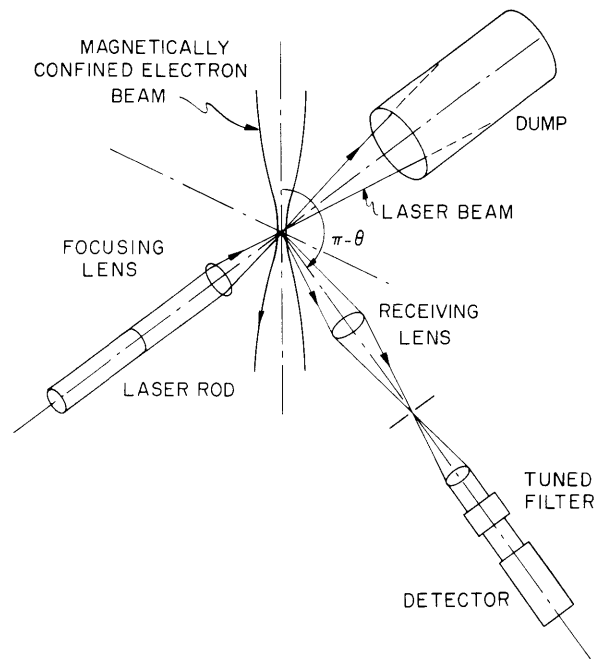
Fig. XIV-4. Simplified diagram of the apparatus.

with respect to this beam. The laser produced bursts of light at 6934 Å of approximately 20 joules and 800-μsec duration. An electron density estimated at ~5 × 10^9 cm^{-3} was produced by magnetically focusing a 2-kv 75-ma electron beam. The polarization of the incident light was adjusted to be parallel to the magnetic field.

The scattered radiation from a volume ~2 mm in diameter was collected by the receiving lens, 20-mm in diameter, at a distance of 80 mm. After passage through an iris (to limit the field of view) and a system of filters, this radiation was detected by a photomultiplier with an S20 response, cooled to liquid-nitrogen temperature. The interference filters enabled us to reject the laser light scattered from the walls of the vacuum system, and to accept only the scattered radiation that was Doppler-shifted 259 Å. The bandwidth was limited to approximately 10 Å in order to reduce the background illumination from the electron gun. Oscilloscope traces of 2-msec duration of the photomultiplier output were obtained for the three cases:

(a) signal plus noise, i.e., the laser beam impinging on the electron beam;

(b) electron-beam noise, i.e., light from the filament plus possible excitation of residual gas by the beam.

(c) laser noise, i.e., the laser light scattered into the receiver in the absence of the electron beam.

As the photomultiplier dark current can be ignored, the sum of the photoelectron counts in (b) and (c) gives the total noise. Hence the difference between (a) and [(b) plus (c)] is

a measure of the signal that is due to Thomson scattering. Many such groups of oscil-
lograms were taken. The average value of this difference and its standard deviation
are tabulated here for three series of trials.

Number of Trials	Average Thomson Photoelectrons	Standard Deviation
15	3.4	1.14
21	1.85	0.90
22	5.8	1.85

The variation in the average count for the three series is thought to be caused by changes
in alignment. Also, in the last series there was a 20 per cent increase in the laser out-
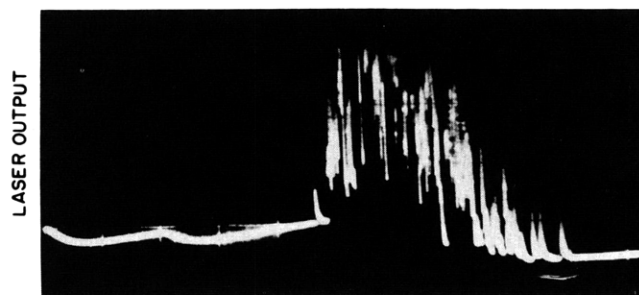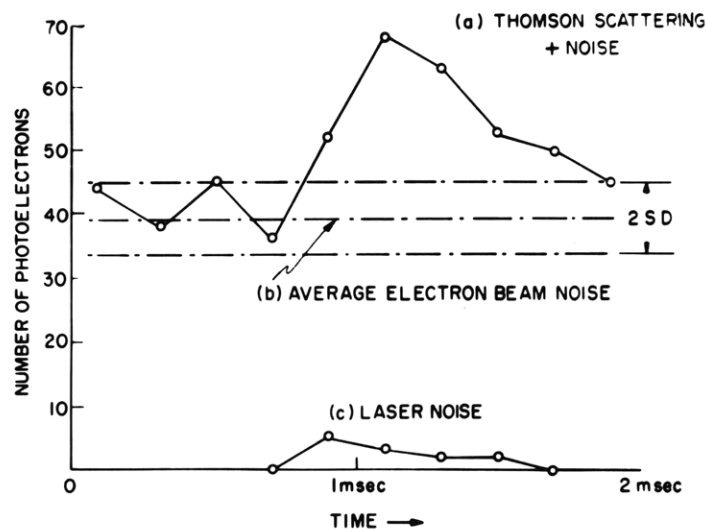put, and the focusing of the electron beam was improved.

Fig. XIV-5. Number of photoelectrons in successive 0.2 msec intervals (summed
over 36 successive trials) resulting from (a) Thomson scattering plus
noise and (c) laser light scattered into the receiver in the absence of
the electron beam. (b) Average electron beam noise and (d) oscillo-
gram of the laser output.

Figure XIV-5 shows for the first two series of trials: (a) the total number of photo-electrons observed in successive 0.2-msec intervals; (b) the average noise level that is due to the electron beam and its standard deviation; (c) the contribution from the "laser noise"; and (d) an oscilloscope trace of the laser output.

The signal-to-noise ratio that we obtained could undoubtedly be improved by pro-viding better trapping for the light from the electron-gun cathode and/or by using a dark emitter instead of the tantalum cathode that we used in our experiment. Also, higher beam current and better focusing should not be too difficult to obtain. Larger laser out-put would, of course, be beneficial because even in this initial experiment the isolation between the two optical paths, input and detector, was sufficiently good that the laser noise was almost negligible. By using this technique, it should be possible to study the profiles of high-density electron beams used, for example, in klystrons and traveling-wave tubes, and as these beams are usually of fairly high voltage, the large transverse Doppler shift will enable observations to be made at right angles to the electron beams.

G. Fiocco, E. Thompson

D. USE OF FISSILE NUCLIDES IN FUSION REACTOR BLANKETS

The investigation of the problem of the fusion reactor blanket with fissile nuclides discussed in Quarterly Progress Report No. 67 (page 91) has been continued. Most of the neutron multiplication and tritium breeding calculations have been finished, and the study of heating in the blanket is in progress. The calculations were made for slab blanket configurations with a diffuse plane neutron source.

1. Blanket Assembly with Th^{232} First Wall

In checking the calculations for the case of the metallic thorium first wall, an error was discovered in the thorium (n, 3n) reaction cross sections, and thus the results reported in Quarterly Progress Report No. 67 (page 92; see Table VIII-2) are incorrect. The results of the calculations based on the corrected cross-section data appear in Table XIV-1; the increase in tritium regeneration is approximately 8 per cent.

Calculations for a blanket assembly with a Th^{232} first wall (Table XIV-2) indicate that increasing the concentration of the lithium 6 isotope in the fused-salt coolant effec-tively reduces the neutron absorption in the first wall. A change in Li^6 concentration from its natural abundance (7.4 per cent) to 50 per cent increases the tritium production from 1.135 to 1.263 tritons per incident neutron for a 2.0-cm thick Th^{232} first-wall configuration. This rise in the regeneration ratio should be sufficient to ensure a self-sustaining tritium cycle for the fusion reactor.

To reduce the heat removal problems that arise because of the large amount of fis-sion energy produced in the thorium, it is desirable to make the first wall as thin as structural and neutronic considerations will permit. Results were obtained for a 1.0-cm

Table XIV-1. Results of thorium first-wall calculations.

Th^{232} first-wall thickness	2.00 cm	1.00 cm	1.50 cm	2.00 cm
Li^6 concentration in both fused-salt regions	natural	50%	50%	50%
Fission rate	0.033	0.018	0.026	0.033
First-wall multiplication	0.372	0.206	0.294	0.373
First-wall absorption	0.261	0.055	0.093	0.134
Total neutron leakage	0.056	0.031	0.029	0.028
Tritium regeneration ratio	1.135	1.183	1.229	1.263

All results are per unit primary source neutron.

Table XIV-2. The three basic blanket configurations considered in this report.

Th^{232} First Wall

Vacuum	First wall Th^{232}	First-wall coolant $66LiF-34BeF_2$	Primary attenuator $21C-79(66LiF-34BeF_2)$	Thermal shield
.	A	6.25 cm	56.0 cm	

Data pertaining to individual calculations are given in Table XIV-1.

U^{238} Fused-Salt First-Wall Coolant

Vacuum	First wall Mo	First-wall coolant $LiF-BeF_2-UF_4$	Primary attenuator $21C-79(66LiF-34BeF_2)$	Thermal shield
	1.0 cm	6.25 cm	49.0 cm	

Data pertaining to individual calculations are given in Tables XIV-3 and XIV-4.

U^{238} Fused-Salt Primary Attenuator Coolant

Vacuum	First wall Mo	First-wall coolant $66LiF-34BeF_2$	Primary attenuator $21C-79(73LiF-27UF_4)$	Thermal shield
	1.0 cm	1.5 cm	49.0 cm	

Data pertaining to individual calculations are given in Table XIV-5.

All compositions are given in mole fraction percentages.

and a 1.5-cm thick first wall with a Li^6 concentration of 50 per cent; the minimum thickness is approximately 1.0 cm. The thickness of the first wall may be reduced further if the loss in the thorium neutron multiplication is compensated for by the addition of metallic beryllium to the attenuator region. (This possibility is discussed below in connection with the uranium fused-salt systems.) But, if the multiplication in thorium is so low that beryllium is needed to supplement it, then the use of thorium in the blanket seems purposeless.

2. Blanket Assembly with UF_4 Fused Salts

The plasma blanket system containing a lithium-beryllium-uranium fluoride fused salt in the first-wall coolant region has been studied for three salt compositions. The effects of increasing the isotopic concentration of Li^6 in the fluoride salt, and of adding metallic beryllium to the primary attenuator have been investigated. A system that contains the uranium-bearing fused salt in the attenuator (third) region also has been explored.

The three salts considered are $73LiF-27UF_4$, $60LiF-30BeF_2-10UF_4$, and $71LiF-16BeF_2-13UF_4$. The first two salts have been described previously[1]; the third mixture is the eutectic composition for a melting point of approximately 450°C.

Calculations indicate that for a first-wall coolant that is approximately 6.25 cm thick and contains uranium (Table XIV-2), a Li^6 concentration of 15-20 per cent is needed in both the first-wall coolant and the primary attenuator to give a tritium regeneration ratio of 1.15. Neutron capture is reduced in both the molybdenum first wall and the uranium in the coolant by the competing $Li^6(n,t)$ reaction; also, a large percentage of the leakage neutrons are utilized for tritium production by this reaction. The maximum tritium regeneration obtained was 1.271 for the $73LiF-27UF_4$ system, with a Li^6 concentration of 50 per cent in both fused-salt regions. The results of these calculations are summarized in Table XIV-3.

In the uranium-containing fused-salt blanket, the production of Pu^{239} for fission reactor fuel may be worth considering.[1] A favorable economic balance between tritium regeneration and plutonium production may be achieved by proper choice of the Li^6 concentration.

The tritium production in the blankets discussed above may be increased by including a region of metallic beryllium between the first-wall coolant and the primary attenuator. Calculations were made for the equivalent of a 5.0-cm thick slab of beryllium homogenized throughout the attenuator region; the results show a gain in the tritium breeding ratio of approximately 5 per cent. This homogeneous treatment was made necessary by the use of the three-region code,[2,3] and the results are conservative. The results are given in Table XIV-4.

The third blanket assembly shown in Table XIV-2 was investigated. Placing the

Table XIV-3. The effect of the Li^6 concentration in the fused salts on the tritium regeneration.

First-wall coolant composition $(LiF-BeF_2-UF_4)$	60-30-10	60-30-10	71-16-13	71-16-13	73-00-27[a]	73-00-27	73-00-27
Li^6 concentration in both fused-salt regions	natural	20%	natural	20%	natural	20%	50%
Fission rate	0.027	0.027	0.036	0.036	0.066	0.063	0.063
U^{238} multiplication	0.120	0.120	0.159	0.159	0.291	0.278	0.278
U^{238} absorption	0.101	0.062	0.122	0.076	0.231	0.144	0.084
Total neutron leakage	0.093	0.066	0.092	0.065	0.088	0.064	0.046
Tritium regeneration ratio	1.070	1.152	1.082	1.172	1.077	1.197	1.271

All results are per unit primary source neutron.

All compositions are given in mole fraction percentages.

[a]These calculations were made with a 6.68-cm thick first-wall coolant region.

Table XIV-4. The effect of adding metallic beryllium to the attenuator region on the tritium regeneration.[a]

First-wall coolant fused-salt composition ($LiF-BeF_2-UF_4$)	60-30-10	73-00-27
First-wall coolant thickness	6.25 cm	6.25 cm
Li^6 concentration in both fused-salt regions	natural	50%
Fission rate	0.027	0.063
U^{238} multiplication	0.120	0.278
U^{238} absorption	0.105	0.088
Total neutron leakage	0.086	0.048
Tritium regeneration ratio	1.141	1.332

The equivalent of 5 cm of beryllium metal is homogenized throughout the primary attenuator.

All results are per unit primary source neutron.

All compositions are given in mole fraction percentages.

[a] Compare with results in Table XIV-3.

Table XIV-5. The results for the calculations with $73LiF-27UF_4$ in the attenuator region.

Li^6 concentration in both fused-salt regions	natural	50%	50%
Beryllium enrichment in third region	0	0	~5.0 cm
Fission rate	0.110	0.109	0.100
U^{238} multiplication	0.449	0.444	0.403
U^{238} absorption	0.655	0.222	0.221
Total neutron leakage	0.120	0.062	0.063
Tritium regeneration ratio	0.751	1.248	1.303

All results are per unit primary source neutron.

73LiF-27UF$_4$ fused salt in the third region gave a tritium production of only 0.751 with natural lithium in the salt; a Li^6 concentration of 50 per cent increased this value to 1.248, and the further addition of the equivalent of 5.0 cm of beryllium to the attenuator region raised the tritium regeneration ratio to 1.303. This configuration has the advantage of distributing the fission energy over a large volume, thus reducing the peak fused-salt temperature and the resultant heat-removal problems. The fission and neutron capture rates are also increased over the corresponding rates in the systems discussed above. Thus, the total power output of the fusion reactor is raised, and a greater amount of Pu^{239} is produced. Table XIV-5 contains the results of the calculations for this blanket system.

3. Discussion

It is possible to obtain sufficient neutron multiplication with both a metallic Th^{232} first wall and a U^{238} fused-salt coolant blanket assembly to support a self-sustaining tritium cycle. Of the systems considered, the thorium first-wall configuration seems to be the least attractive because (a) the fission energy is liberated in a structural member that is already at a high temperature by virtue of its location, and thus the cooling problem is increased; (b) the build-up of fission products will decrease its effectiveness in neutron multiplication; and (c) radiation and fission damage may reduce its value as a structural support for the blanket assembly.

The uranium fused-salt systems seem practical and feasible because (a) the fission heat is deposited in the coolant itself; (b) fission products can be extracted continuously from the circulating fused salt; (c) the concentration of the uranium fluoride can be varied to control the power output; and (d) an economic balance between tritium regeneration and Pu^{239} production might be achieved by varying the Li^6 concentration in the fused salt.

L. N. Lontai, D. J. Rose, I. Kaplan

References

1. L. N. Lontai and A. J. Impink, Use of fissile nuclides in fusion reactor blankets, Quarterly Progress Report No. 67, Research Laboratory of Electronics, M.I.T., October 15, 1962, pp. 91-94.

2. W. G. Homeyer and A. J. Impink, Energy extraction blanket for a fusion reactor, Quarterly Progress Report No. 64, Research Laboratory of Electronics, M.I.T., January 15, 1962, pp. 128-131.

3. W. G. Homeyer, A. J. Impink, and D. J. Rose, Energy extraction blanket for a fusion reactor, Quarterly Progress Report No. 66, Research Laboratory of Electronics, M.I.T., July 15, 1962, pp. 142-150.

E. DESIGN AND CONSTRUCTION OF A LARGE PLASMA FACILITY

A facility whose design and construction was started by S. O. Dean (a former student) has now been completed. The machine provides a high-vacuum volume of 23 liters and has a pumping capacity of 500 μ-l/s in the pressure range $10^{-2} \div 10^{-3}$ Torr. Solenoid coils can produce a mirror region in the vacuum tank which measures 1.25 meters and 0.20 meter I.D. with mirror ratio $R \approx 5$ and mirror field ~3.2 kgauss at 200 amps. The mirror ratio can be varied by moving the two solenoids on rails. In the present use, the machine is arranged for a hollow-cathode discharge experiment running longitudinally in the mirror. (See Fig. XIV-6.) A special probe was designed for related measurements.

The high-vacuum tank consists of a central box ($50 \times 50 \times 25$ cm) and two cylindrical,
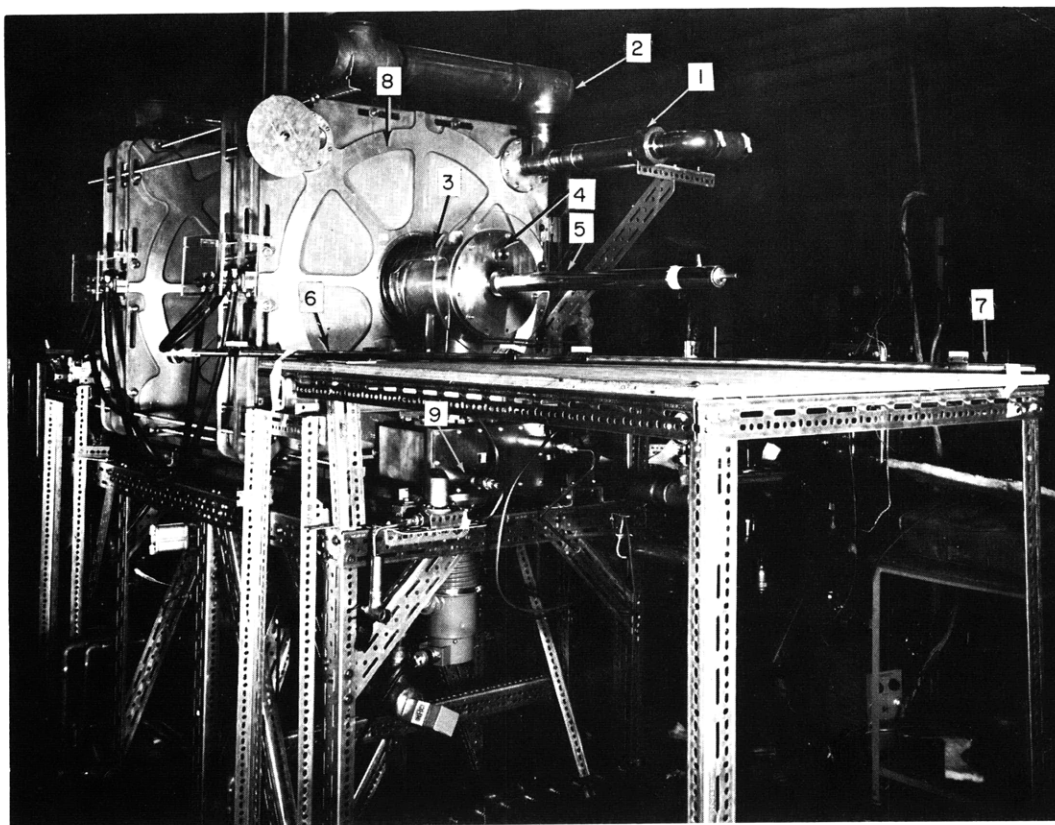

Fig. XIV-6.   Plasma facility from anode end.   (1) Magnet cooling-loop sliding seal. (2) Cooling-loop expansion tank. (3) High-vacuum tank extension. (4) Position of sliding seal for probe. (5) Anode electrode, inserted in tank through sliding seal. (6) and (7) Probe holder inside its coaxial rail; the four visible insulated supports fasten the rail to the vacuum tank's inside wall. (8) Magnet. (9) Baffle on top of one of three diffusion pumps.

20-cm I.D. arms, extending longitudinally through the mirror coils. Three extensions, 15-cm I.D., connect the tank to the diffusion pumps that are topped by water-cooled baffles and gate valves. Cooling of the side arms is achieved by water circulation (Fig. XIV-7).
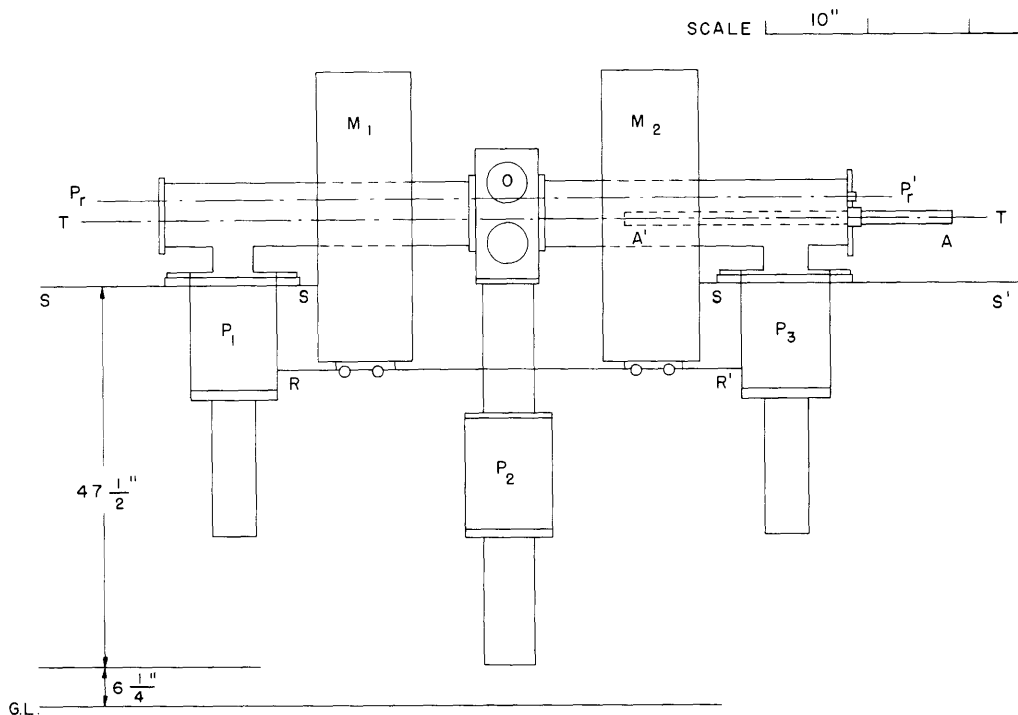

Fig. XIV-7. Assembly. AA', anode (cathode not shown); M_1M_2, magnet coils; O, observation ports; $P_1P_2P_3$, diffusion pumps and baffles; P_rP_r', probe-holder axis; TT', mirror axis; RR', magnet rails.

Each of the two solenoids consists of four aluminum double pancakes, 73-cm outside radius, and 5 cm thick. The pancakes are spaced 1.25 cm apart and are connected externally in series and are contained and supported along one diameter by a cast aluminum box (85 × 85 × 25 cm).

The coolant is circulated from the top to the bottom of the assembly and in direct contact with the coils. Pure distilled water or ethylene glycol is used. The circulation is in a closed loop, and a heat exchanger is installed in series with it; city water is used for heat removal. To enable movement of the magnets, sliding O-ring seals are installed in the cooling loop.

The electrodes for the hollow-cathode discharge are of standard design,[1] but more care than usual was taken in cooling the tips. These are almost entirely hollow and

contain two rows of fins to improve the heat removal.   Water is circulated in through a peripheral sleeve, and out axially.   The electrodes can slide axially through O-ring seals in the end flanges of the side arms.   The power supply consists of two AIRCO welding rectifiers in series, giving 200 amps at 80 volts under load.   A spark-gap oscillator is included in the circuit as starter; a filter reduces the ripple to less than 1 per cent.

To probe the hollow-cathode discharge, whose maximum length can be 1.6 meters, Langmuir probes are used.   Two of these, rigidly connected, are installed; they can be moved parallel to the mirror axis and rotated in a normal plane.   The probe tip describes a circular path, 45° wide, through the mirror axis.   The probes are placed 75 cm apart on a supporting arm 1.9 meters long.   Each probe tip can span 80 cm of the arc; overlap of the two probe positions allows for reciprocal calibration.   The movement is imposed from the outside through a sliding O-ring seal in the end flange.   The stainless-steel holder arm contains and seals the probe leads; it is longitudinally supported in the tank by a coaxial cylindrical rail, 2.0 meters long.   The rail also serves as screen against the sputtering from the arm.

F. Alvarez de Toledo

References

1. W. D. Getty, A low-pressure gas-arc discharge, Quarterly Progress Report No. 57, Research Laboratory of Electronics, M.I.T., April 15, 1960, pp. 27-29.

F. ENERGY EXTRACTION BLANKET FOR A FUSION REACTOR

Work on nonfissile systems has been completed and final reports are being prepared as theses[1,2] for submission to the Department of Nuclear Engineering, M.I.T.

Heating calculations have revealed that each 14.2 Mev D-T neutron will produce approximately 17.5 Mev of recoverable heat in the blanket.   The maximum energy flux of 14.2 Mev neutrons that can be tolerated on a 2-cm molybdenum first wall is 4-5 Mw/m^2.   Thermal stress and heat transfer to a fused Li_2BeF_4 coolant are both limiting at this power.   The total blanket thickness necessary to shield superconducting coils is 110-120 cm.

W. G. Homeyer, A. J. Impink, Jr., D. J. Rose, I. Kaplan

References

1. W. G. Homeyer, Thermal and Chemical Aspects of the Thermonuclear Blanket Problem, Sc.D. Thesis, Department of Nuclear Engineering, M.I.T., December 1962.

2. A. J. Impink, Jr., Neutron Economy in Fusion Reactor Blanket Assemblies, Ph.D. Thesis, Department of Nuclear Engineering, M.I.T., January 1963.

G. SUPERCONDUCTING SOLENOID

1. Test of a Large Superconducting Coil

While the construction of the vessel and accessories of the large superconducting magnet[1] is progressing satisfactorily, we have proceeded to test a set of three coils in order to evaluate and choose the best design to be used for the remaining coils of the larger magnet. We have also developed an IBM 7090 computer program for the calculation of the magnetic field in any coil or set of coils.

The three coils have been tested in a vertical 14.00-in. liquid-helium dewar.[2] Figures XIV-8, XIV-9, and XIV-10 show close-up views of the coil X1 alone, the set of three coils, and the coil assembly with the dewar.

The specifications of the coils are given in Table XIV-6. Their differences are essentially in the winding, which for the coil X1 was made by using insulated Nb-Zr wire; some copper wire was wound inside and outside for the purpose of protection. For coil X2, the same insulated superconducting wire was used, but it was wound with bifilar copper magnet wire. Finally, coil X3 was made by using insulated copper-plated Nb-Zr, 0.0012 in. thick. No secondary copper winding was used. Figure XIV-11 shows the detail of the winding of coil X1.

Coil X1, which was ready first, underwent the most intensive testing, both alone and with the two other coils.

Intensive investigation of the quenching characteristics has been carried out in order to find the eventual training effect, deterioration of the critical current of the coil and energy balance in the various circuits, as well as the quenching current.

The listings in Table XIV-6 also indicate that the training effect was nonexistent for the three coils and, moreover, that the quenching current is not associated with the rate at which the current is increased (from 20 seconds to 5 minutes for a full increase). For coils X1 and X3 no deterioration of their properties was observed, although the energy involved became quite large (5 kilojoules with the three coils running). The recovery time after quenching is approximately 20 seconds. The deterioration of coil X2 has been found to be due to a kink in the wire which progresses up to a complete break.

The transient phenomena that occur at quenching have been recorded with an oscilloscope for coil X1 only. We have not been able to record the transient in coil X3, probably because of too small a rate of quenching. Figures XIV-12 and XIV-13 illustrate the basic process of quenching. For a single winding, the current decay is approximately 0.030 second. When two windings are separately driven, there is quite a big delay (0.260 sec) between the quenching of the two coils.

By integration of the transient curve of the copper coil, one can calculate the energy that has been dissipated in its external resistance (3 ohms). It appears that in our case only 2 per cent of the magnetic energy has been dissipated into the external resistance.

Table XIV-6. Coil data and results of the tests.

	X1			X2			X3	Notes
	inner	outer	total	inner (bifilar)	outer	total	total (copper-plated)	
I.D. (in.)	11.562	12.584	11.562	11.390	12.696	11.390	11.390	
Turn spacing	0.0124	0.0127	0.0126	0.0257	0.0116	(0.0190)	0.0144	( ) average value
Layer spacing	0.020	0.020	0.020	0.0172	0.022	(0.0202)	0.0242	
Space factor (%)	31.7	30.9	31.2	17.8	30.5	(20.4)	22.5	Length of each
Turns	1841	2740	4581	2580	1661	4241	4449	winding: 1.750 in.
Length of wire (ft)	5745	9363	15109	8419	5738	13757	14930	
Quenching current								
Minimum	20.0	16.0	15.1	15.1	16.0	11.5	20.0	
Maximum	22.7	19.0	16.7	18.5	18.5	15.5	22.0	
Average	22.0	18.0	16.0	(17.0)	(17.0)	(15.0)	21.5	
B av quench (kg) (central field)	0.818	1.880	2.880	1.080	1.780	2.500	3.750	
Number of quenches	46	10	57	8	10	10	10	
Training	No	No	No				No	
Deterioration	No	No	No			Yes	No	

Maximum field recorded with the three coils running together. 5,600 kgauss on the axis, that is, 11,000 gauss on the edge of the coil.
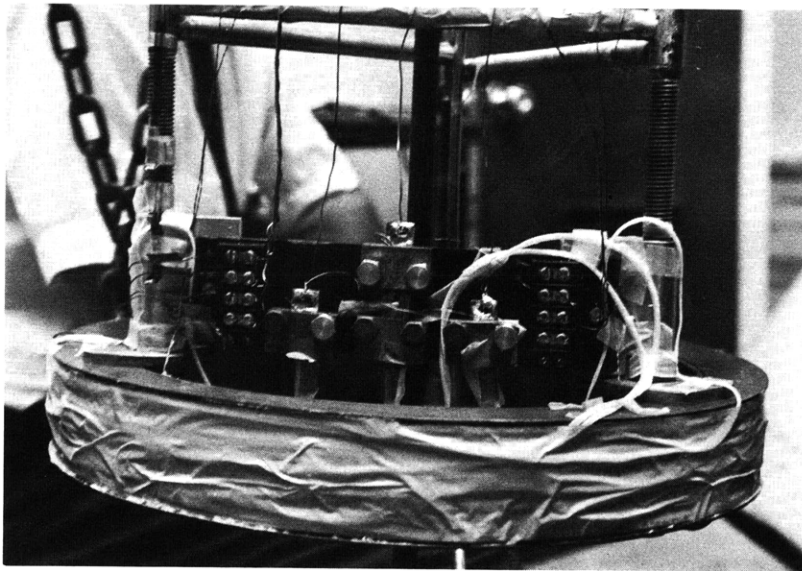
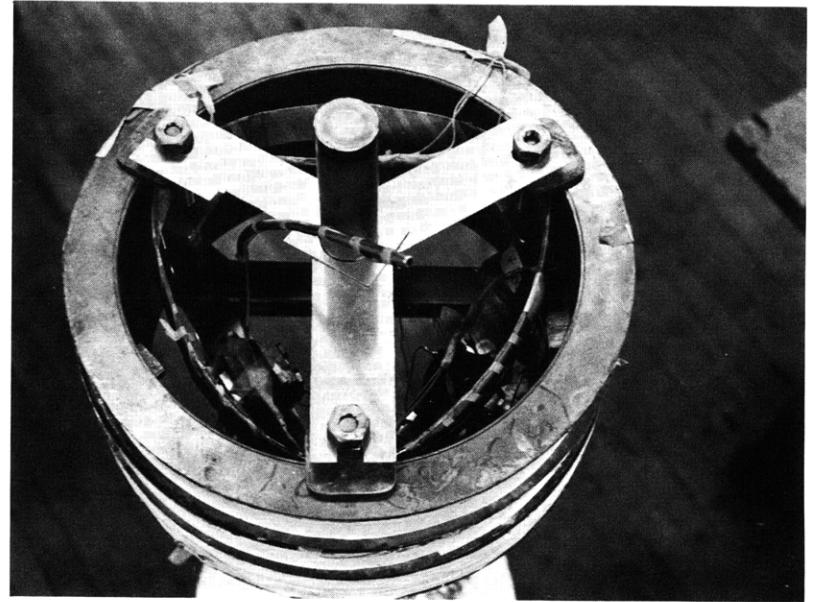Fig. XIV-8. Coil X1 with its connections.

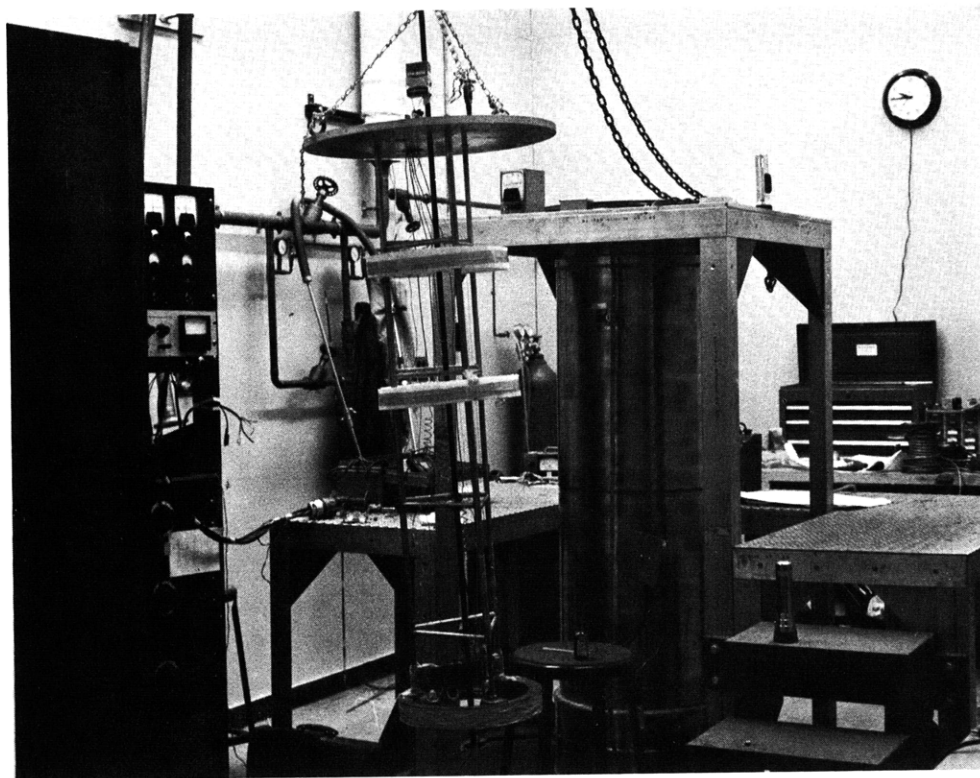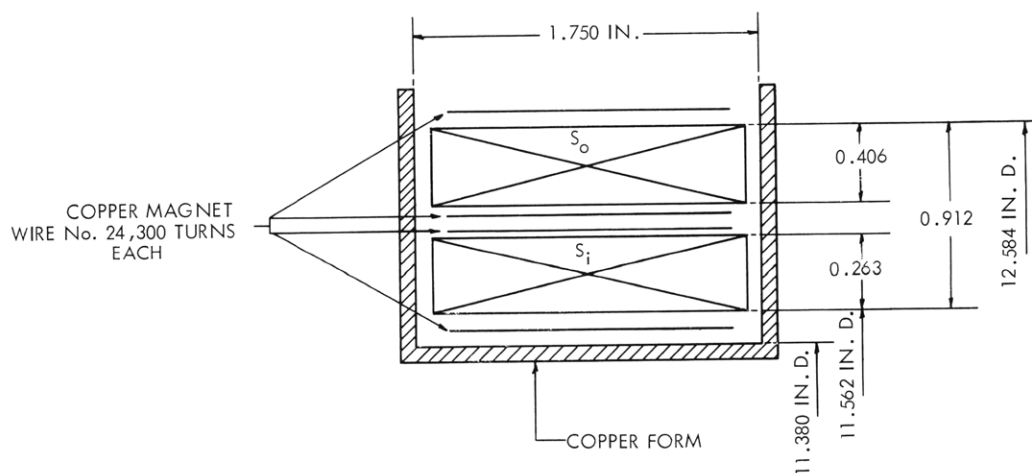Fig. XIV-9. Three-coil arrangement with the terminal switches inside the coils.

Fig. XIV-10. Coil X1 with its support, the 14-in. dewar.

COPPER MAGNET WIRE No. 24,300 TURNS EACH

1.750 IN.

0.406

0.912

0.263

12.584 IN. D.

11.562 IN. D.

11.380 IN. D.

COPPER FORM

S_i INSIDE SUPERCONDUCTING WINDING - 1841 TURNS IN 13.13 LAYERS SEPARATED WITH 0.075 IN. MYLAR FOIL SPACE FACTOR 31.7%- 5745 FT.,1.681 LBS. OF Nb-Zr WIRE

S_o OUTSIDE SUPERCONDUCTING WINDING - 2740 TURNS IN 20.27 LAYERS SEPARATED WITY 0.075 MYLAR FOIL SPACE FACTOR 30.9%- 9363 FT.,2.816 LBS OF Nb-Zr WIRE

ALL THE WINDING IS ENCAPSULATED INTO AIR-DRY VARNISH (No.=301 OF PEDIGREE COMPANY)

Fig. XIV-11. Schematic cutaway of the winding
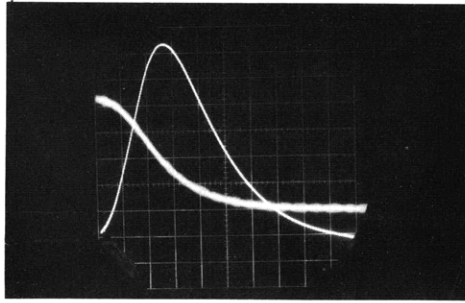of the X1 coil.

Fig. XIV-12. Quenching transient for inner coil. The bell-shaped curve is the voltage (across a 3-ohm resistor) of the current in the copper coil. Scale, 5 volts/cm. The other curve is the decay of the superconducting current, 5 amp/cm. Time scale, 5 msec/cm. Quenching time, 30 msec.
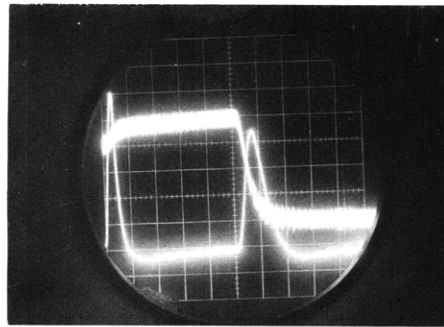

Fig. XIV-13. Quenching transient for the two windings in parallel. The curve with two peaks is for the copper coil (5 volts/cm across 3 ohms). Other curve is for the current in the inner coil (5 amps/cm). Time scale, 50 msec/cm. Quenching occurs in 2 steps: first, the outer coil quenches and current rises in the inner coil; second, after 0.260 sec the inner coil quenches. Each quenching takes approximately 30 msec.

This is due certainly to the large energy dissipation in the copper coil form, which was detected by a quick rise of its temperature.

The behavior of the copper-plated coil, X3, was found to be much more satisfactory than that of the two other coils in all respects. Its operation seems more stable, and it is possible to reach and maintain the current within a few per cent of the maximum value of the current. Moreover, its performances are approximately 30 per cent better than those of the other coils. Consequently, all of the remaining coils will be made of copper-plated wire similar to that used for coil X3.

The coils have been operated in the permanent current states, and differential
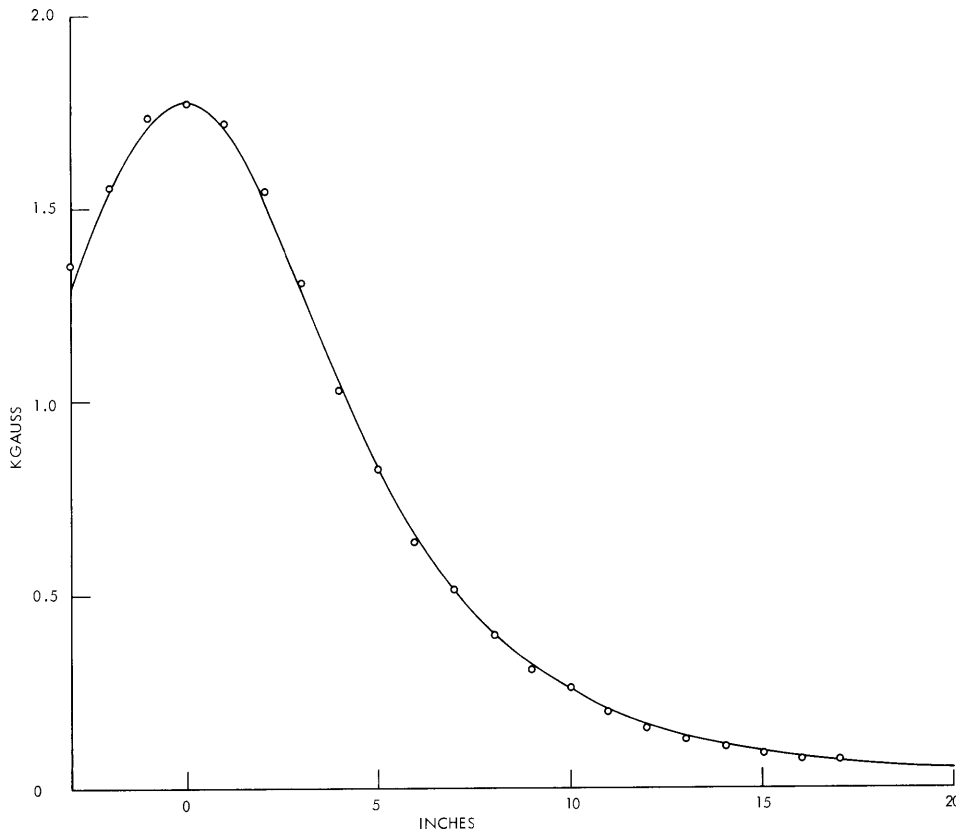
Fig. XIV-14. Field plot of coil X3 in permanent state. Current, 10 amps. The curve
represents calculated values; measured values are plotted as o.

measurement of the magnetic field leads to the conclusion that there is no decay of the field (say, less than 10^{-4} per hour measured). The field plot measured in the permanent current state is shown in Fig. XIV-4 with the calculated value. The thermal switches operate very satisfactorily. Their power consumption is 0.150 watt for warming up the gate wire to the critical temperature, and their switching takes approximately 1 second.

We have been able to pump the field from the X3 coil to the X1 and X2 coils by using the proper switching sequence in and out of the permanent mode. The highest field produced has been achieved in this way.

The clamped contacts have shown a contact resistance of the order of 10^{-7} ohms, which is also quite satisfactory.

2. Magnetic Field Calculation

An IBM 7090 computer program has been developed[3] for the calculation of both components of the magnetic field at any location of a solenoid, including the winding interior.
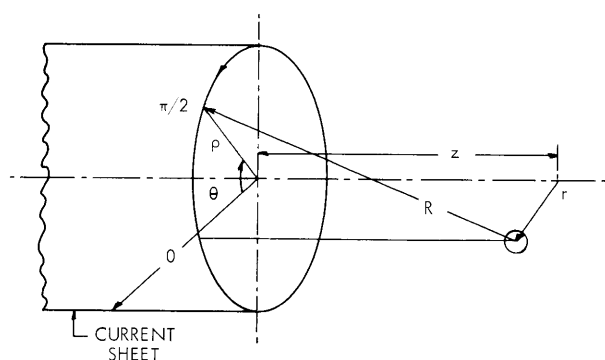
Fig. XIV-15. Coordinates used in calcula-
tion of the magnetic vector
potential and magnetic field
for a cylindrical geometry.

The program was then extended to calcu-
late for a multicoil solenoid, for the
reciprocal case of the determination of
the current that will produce a given
magnetic-field shape, and for the field of
a uniformly distributed dipole in a sole-
noidal winding. All three cases are impor-
tant for the evaluation of the performance
of superconducting solenoids.

The principle of these field calcula-
tions is based on the splitting of the
winding in several current sheets. We
assume a uniform distribution on the cur-
rent throughout the winding. It can be
noted, then, that the program can be easily modified to fit any current distribution by
weighting each current sheet accordingly.

The field is derived from the expression of the vector potential of a current loop[4-7]

$$A(r, z) = \frac{1}{2\pi} \int_0^\pi \frac{\cos \theta}{R} \, d\theta, \tag{1}$$

where R is the distance between the field point and the source point as shown in
Fig. XIV-15:

$$R = [r^2 - 2r \cos \theta + 1 + z^2]^{1/2}. \tag{2}$$

The distances are normalized to the radius of the current sheet, and the vector
potential (and subsequently the field) to the value of an infinitely long solenoid, that is,
$\left(\mu \frac{NI}{L} \text{ in mks units or } \frac{4\pi}{10} \frac{NI}{L} \text{ in cgs units} \right)$.

For a current sheet extending from $z = S_1$ to $z = S_2$, the magnetic potential is

$$S(r, z) = \frac{1}{2\pi} \int_{S_1}^{S_2} \int_0^\pi \frac{\cos \theta}{R} \, d\theta ds. \tag{3}$$

If the order of integration is inverted, the integration with respect to S carried out,
the angular integration modified by using the identity

$$\int_0^\pi F(\cos \theta) \, d\theta = \int_0^{\pi/2} F(\cos \theta) \, d\theta + F(-\cos \theta) \, d\theta, \tag{4}$$

and the origin S_1 extended to infinity, one obtains the vector potential of a semi-infinite
current sheet:

$$A(r, z) = \frac{1}{2\pi} \int_0^{\pi/2} d\theta \cos \theta \ln \frac{z + \sqrt{z^2 + r^2 + 1 + 2r \cos \theta}}{z + \sqrt{z^2 + r^2 + 1 - 2r \cos \theta}} \tag{5}$$

The radial and axial magnetic fields are derived from the vector potential and are given by

$$H_r(r, z) = -\frac{\partial A(r, z)}{\partial z} \tag{6}$$

$$H_z(r, z) = \frac{1}{r}\frac{\partial}{\partial r}(rA(r, z)), \tag{7}$$

which, applied to Eq. 5, give

$$H_r(r, z) = \frac{2}{\pi} r \int_0^{\pi/2} \frac{\cos^2 \theta \, d\theta}{Q_+ Q_- (Q_+ + Q_-)} \tag{8}$$

and

$$H_z(r, z) = \frac{1}{2\pi} \int_0^{\pi/2} d\theta \cos \theta \left[\frac{1}{r} \ln \frac{z + Q_+}{z + Q_-} + \frac{2 \cos \theta}{(z+Q_+)(z+Q_-)(Q_+ + Q_-)} \right.$$
$$\left. \times \left(\left(\frac{z^2 + 1 - r^2}{Q_+ Q_-} \right)(z+Q_+ + Q_-) + z \right) \right]. \tag{9}$$

Here,

$$Q_+ = \sqrt{z^2 + r^2 + 1 + 2r \cos \theta} \tag{10}$$

$$Q_- = \sqrt{z^2 + r^2 + 1 - 2r \cos \theta}. \tag{11}$$

The field of a finite current sheet is obtained by superposition of negative and positive semi-infinite sheets:

$$H_{sol}(r, z) = H_{(r, z)} - H_{(r, z+s)},$$

where s is the normalized length of the solenoid.

From the basic current sheet calculations, the field is obtained by summation of current sheets.

$$H(r, z) = \sum_{n=1}^{N} H(r_s(n), z)/N, \tag{12}$$

where $r_s(n)$ is the relative radial distance of the field point with respect to the particular current sheet.

$$r_s(n) = r/\rho(n). \tag{13}$$

Several problems arise in the evaluation of the integrals. For z negative and $\theta = 0$, $Q_- = |z|$, so that $(z+Q_-) = 0$ and the integrand of H_z becomes infinite. This inconvenience is solved by using the following identity proper to a semi-infinite current sheet

$$\begin{array}{ll} r < 1.0 & H_z(r, -z) = -H_z(r, z) + 1.0 \\ r = 1.0 & H_z(r, -z) = -H_z(r, z) + 0.5 \\ r > 1.0 & H_z(r, -z) = -H_z(r, z) \end{array} \right\} \tag{14}$$

93

For z = 0

$r < 1.0$ $H_z(r, 0) = 0.5$

$r = 1.0$ $H_z(r, 0) = 0.25$ (15)

$r > 1.0$ $H_z(r, 0) = 0.0$

Also, $H_r(r, z) = H_r(r, -z)$.

When $|r-1|$ and z both approach zero, the integrands of both H_r and H_z become very large when θ is small; indeed $Q_- \rightarrow 0.0$ for $|r-1|$, z, and $\theta \rightarrow 0.0$. Therefore, in order to conserve accuracy in the numerical integration, it has been found necessary to split the integration with emphasis in the range of $\theta \approx 0.0$. Various test runs, comparing the calculated values with those of Alexander and Downing,[6] have shown that the best accuracy was obtained with a three-part splitting, that is,

$$\int_0^{\pi/2} = \int_0^{0.0625} + \int_{0.0625}^{0.250} + \int_{0.250}^{\pi/2}$$

and by calculating Q_- as

$$Q_- = \sqrt{z^2 + (r-1)^2 + 4r \sin^2 (\theta/2.0)} \qquad (16)$$

In such a way, an accuracy of the order of 10^{-6}, or better, can be maintained for $|r-1.0|$ and $|z| \geq 0.0005$, that is, well below any dimension of the wire used. The change from the single integration to a triple integration must occur in the vicinity of $|r-1.0|$ and $|z| \approx 0.4$.

Nevertheless, for $r = 1.0$ and $z = 0.0$, $H_r(1.0, 0.0) = \infty$. However, this is a purely mathematical conclusion, since, by definition, the thickness of the current sheet is zero, and the corresponding current density is infinite, a situation that never arises physically. To avoid such improper physical results, we stop the current sheet a distance ϵ from the corner, ϵ being less than the physical dimension of the actual current carrier. The use of a Gaussian integration procedure achieves the same purpose, since the lowest value of θ employed is not zero.

Finally, for $r = 0.0$, and for any z, the integrand of $H_z(r, z)$ again behaves badly for computation. However, in that case the field is calculated directly by integration of the Biot–Savard law for a thick solenoid of uniform current density.

$$H_z(0, z) = \frac{1}{2.0(a-1)} \left[(\beta-\gamma) \ln \frac{a + \sqrt{a^2 + (\beta-\gamma)^2}}{1 + \sqrt{1 + (\beta-\gamma)^2}} + (\beta+\gamma) \ln \frac{a + \sqrt{a^2 + (\beta+\gamma)^2}}{1 + \sqrt{1 + (\beta+\gamma)^2}} \right] \qquad (17)$$

See Fig. XIV-16 for definitions of a, β, and γ.

$$\alpha = \frac{D_o}{D_i} \qquad\qquad \beta = \frac{L}{D_i} \qquad\qquad \gamma = \frac{2.0\,z_i}{D_i}$$
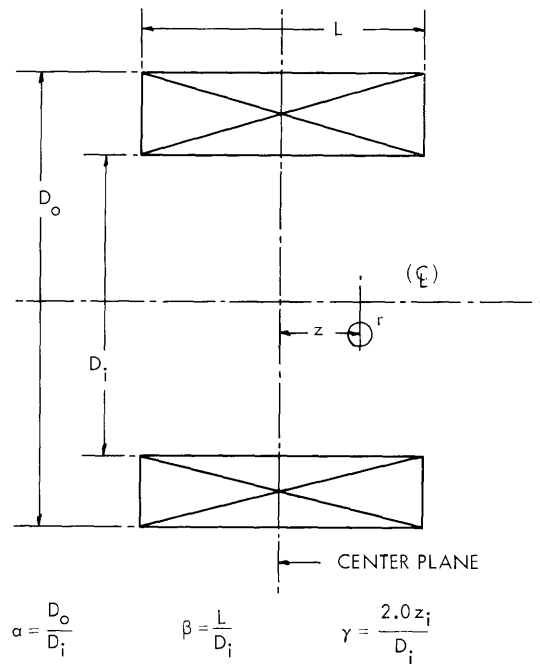
Fig. XIV-16.   Configuration of a thick solenoid.

For a thin solenoid, $\alpha = 1.0$, and Eq. 17 becomes indeterminate. We replace it by the equation for the on-axis field of a current sheet

$$H_z(0,z) = \frac{1}{2.0}\left[\frac{\beta + \gamma}{\sqrt{1 + (\beta+\gamma)^2}} + \frac{\beta - \gamma}{\sqrt{1 + (\beta-\gamma)^2}} \right]. \tag{18}$$

Again, the field is normalized to the field of an infinitely long solenoid.

The program automatically provides selection between the various computation schemes so that the best accuracy and speed is obtained.

The numerical integration of Eqs. 2, 3, and 16 is carried out by a 10-point Gaussian quadrature. Test runs indicate that the accuracy is better than a 16-point Gaussian quadrature, probably because of less rounding-off error during the computation.

For a thick solenoid the accuracy may depend upon the number of current sheets in which the actual winding is split. When the field location is far away from the winding, fewer current sheets are required than when it is very close or inside the winding. There is no definite rule for selecting the optimum number of currents, and accuracy test runs must be made for each particular case. However, let us say that our results indicate that for a thin solenoid, that is, with thickness approximately 10 per cent of the radius, an accuracy of 10^{-5}, or better, is obtained with 5 current sheets for $r < 0.5$, and 10 current sheets for $r < 0.95$. Inside the winding, higher-order splitting is necessary, to approximately the same number as the physical number of layers,

that is, from 20 to 30.

The results also have been compared with those obtained by spherical harmonic expansion.[8,9] We have found that using three terms of the expansion gives only 10^{-3} accuracy within 15 per cent of the radius for the z component, and very much less for the r component. The discrepancy between the two methods increases quickly when r > 0.5, and no comparison can be made for r $\geq$ 1.0 because of nonconvergence of the harmonic expansion.

The basic computation is carried out in a subprogram that calculates H_z and H_r when called by a main program or subprogram. The input data of the subprogram are the inside diameter of the solenoid, the winding thickness, the solenoid length, the number of current sheets in which the winding is split, and the radial and axial field position with respect to the center of the solenoid.

The basic time to calculate the contribution of one current sheet to the H_r and H_z fields takes approximately 0.05 second on the IBM 7090 computer.

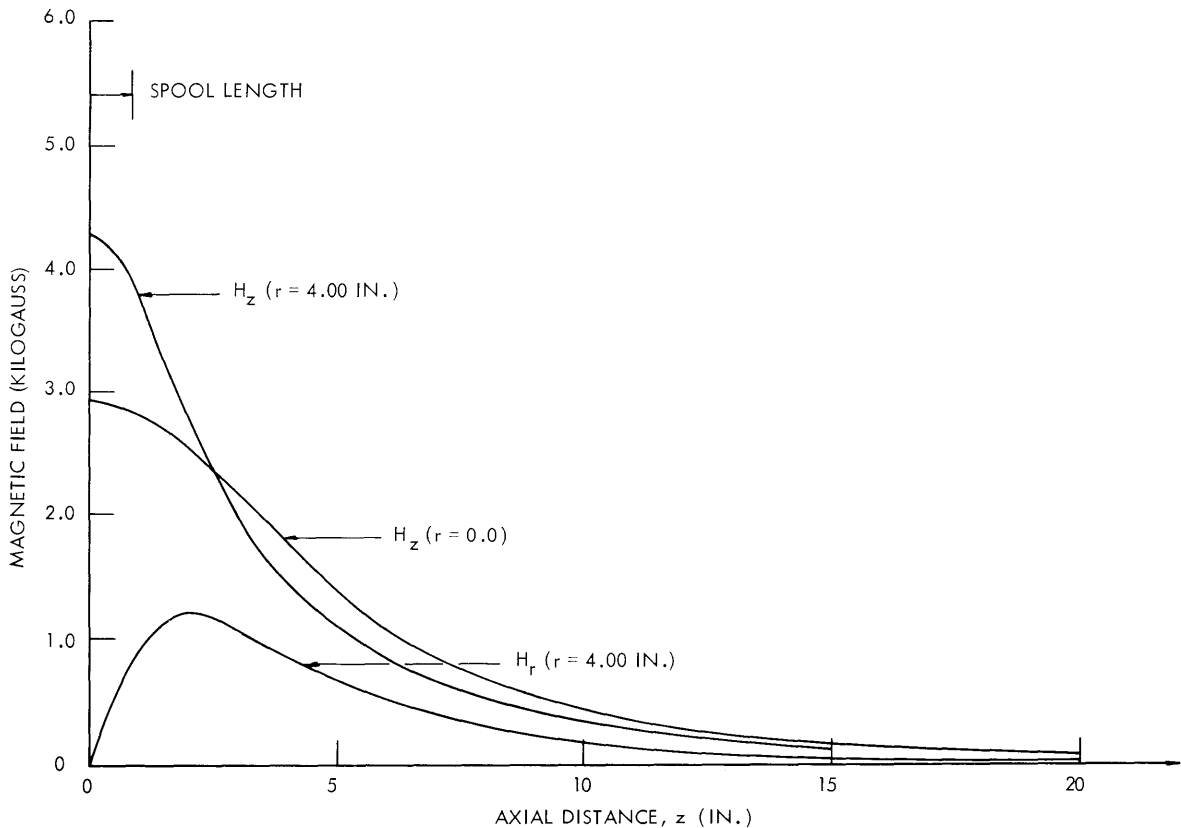Consequently, for a field position that is far enough away from the winding so that

Fig. XIV-17. Field variation along the axis for coil X1.
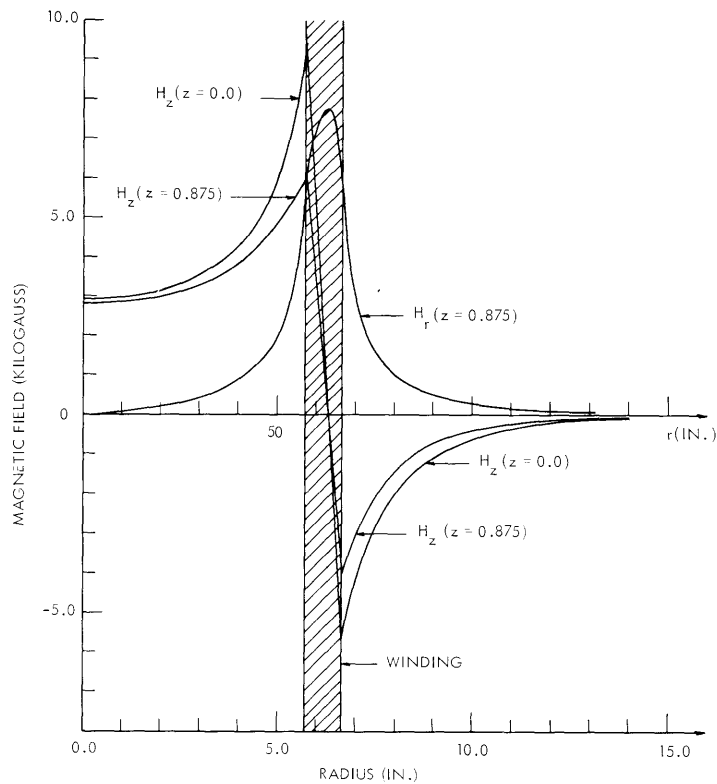$\alpha = 1.158; \beta = 0.151$.

Fig. XIV-18. Field variation along the radius for coil X1.
$a = 1.158;$ $\beta = 0.151.$ $Z = 0.875$ is at the
edge of the winding.

the integration is not split, that is, $|r-1|$ or $|z| > 0.4$, with the use of 5 current sheets,
assumed the result is 0.25 second per point. If the field position is close to the edge
of the winding, then the computation time is approximately three times longer. For
any on-axis point, the use of Eq. 17 or Eq. 18 saves much more time and reduces the
computation time to approximately 0.005 second.

We have applied the basic subprogram for the calculation of the field of a single sole-
noid and also for more complex problems.

For a multicoil solenoid, we simply used a summation of the two components of the
field. Each coil is characterized independently.

$$H_{set}(r, z) = \sum_{i=1}^{P} H_{coil}(r, z_{(i)}) \times \frac{N_{(i)} J_{(i)}}{L_{(i)}}, \tag{19}$$

where $N_{(i)}$ is the number of turns, $J_{(i)}$ the current or current ratio, and $L_{(i)}$
the length of the ith coil.

The inverse problem consists in the determination of $J_{(i)}$ so that the field satisfies

97
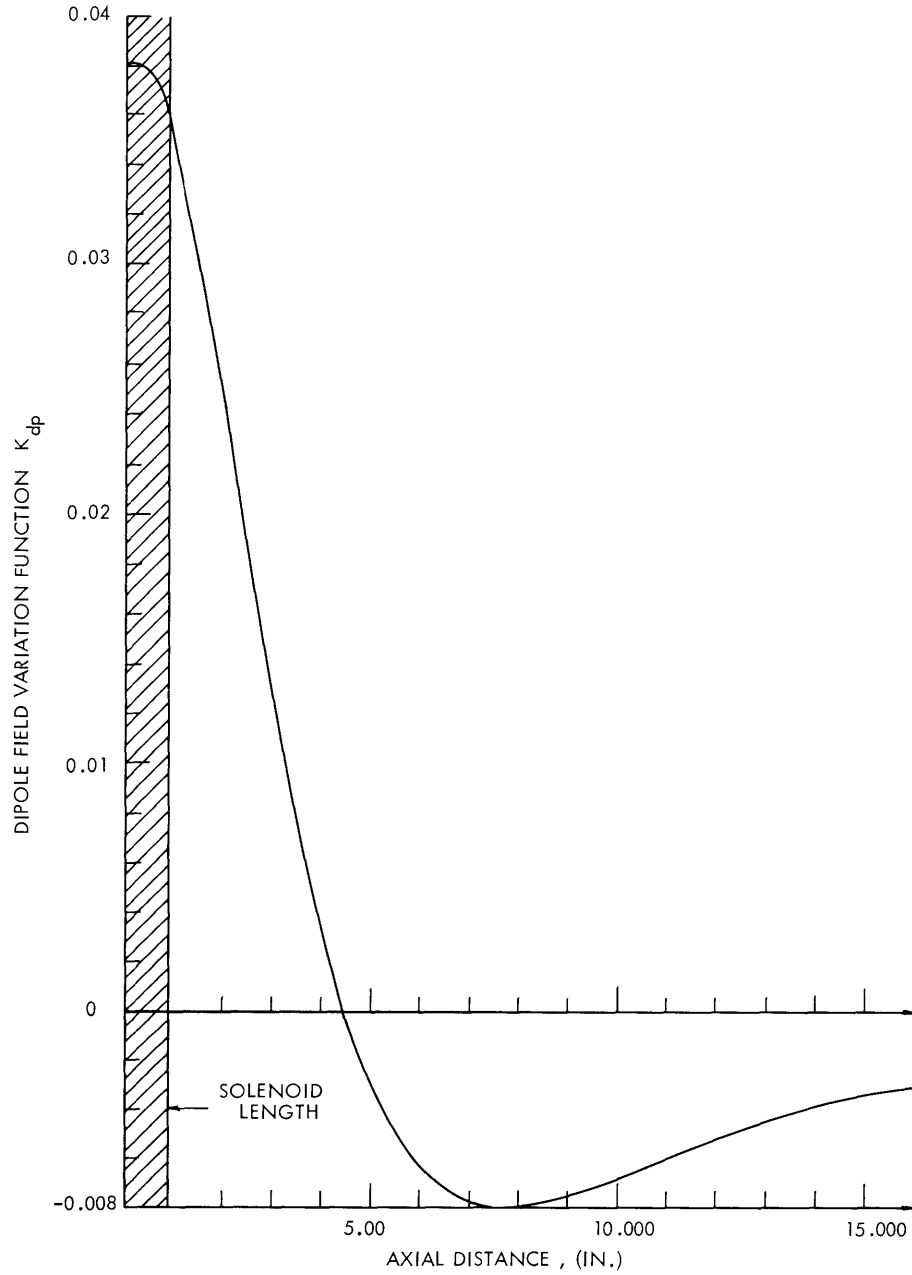
Fig. XIV-19. Axial dipole field of uniformly distributed dipoles in solenoid X1. $H_{gauss} = K_{dp} \times 19.3257 \times I_{amp}$. I_M = equivalent magnetization current.

a given value at P given positions. We have to solve the matrix equation

$$H_{(P)} = K_{(P, N)} J_{(N)};$$ (20)

thus

$$J_{(N)} = K^{-1}_{(P,N)} H_{(P)}.$$ (21)

This operation is easily carried out by the computer. Our program has been set to permit solving this problem when any series grouping of coils is devised.

Dipoles induced into a superconducting solenoid may be of prime importance for the limitation of the current into superconducting solenoids.[10] If we assume uniform distribution of dipoles throughout the winding, the magnetic field results from the superposition of two current sheets of equal strength of opposite direction, one along the inner diameter and the other along the outer diameter.

$$H_{dp} = H_{inner}(r,z) - H_{outer}(r,z)$$ (22)

The normalization factor of the field in that case is

$$K_{dp} = \mu \frac{I_M}{St} = \mu \frac{N_L}{L} I_M,$$ (23)

where St is turn spacing, N_L the number of turns per layer, L the length of the solenoid, and I_M the equivalent magnetization current.

For purposes of illustration we show in Figs. XIV-17, XIV-18, and XIV-19 the fields profiles and denote the field for the X1 coil which is described in the first part of this report.

L. J. Donadieu

References

1. L. J. Donadieu and D. J. Rose, Paper K4, International Conference on High Magnetic Fields, Massachusetts Institute of Technology, November 1-4, 1961.

2. We wish to thank Dr. Z. J. J. Stekly of the AVCO Everett Research Laboratories for the use of the dewar.

3. This work was partly done at the Computation Center, M. I. T.

4. W. R. Smythe, Static and Dynamic Electricity (McGraw-Hill Book Company, Inc., New York, 1950), p. 270.

5. C. Snow, Magnetic Fields of Cylindrical Coils and Annular Coils, National Bureau of Standards, Applied Math. Series, Paper No. 38, 1953.

6. N. B. Alexander and C. P. Downing, Tables for a Semi-Infinite Circular Current Sheet, ORNL-2828, October 13, 1959.

7. E. Durand, Electrostatique et Magnetostatique (Masson Companie, Paris, 1953).

8. D. B. Montgomery and J. Terrell, Some Useful Information for the Design of Air-Core Solenoids, AFOSR-1525, November 1961.

9. M. W. Garrett, J. Appl. Phys. 22 (1951).

10. D. B. Montgomery, Current Carrying Capacity of Superconducting Nb-Zr Solenoids, AFOSR-3015, National Magnet Laboratory, M. I. T., July 1962.